university of groningen / faculty of science and engineering

Search for Hidden Persistent Spin Texture in Bulk $PdSe_2$

Author:
Joan BAUZA FONT
(s5047684)

First examiner:
prof. Jagoda SLAWINSKA
Second examiner :
prof. Maxim MOSTOVOY
Supervisors:
Kilic, S.B. & K. Tenzin

Bachelor's Thesis
To fulfill the requirements for the degree of
Bachelor of Science in Physics
at the University of Groningen

July 9, 2025

Abstract

This study confirms the existence of a hidden persistent spin texture in bulk $PdSe_2$, a centrosymmetric layered material, through first-principles density functional theory (DFT) calculations. Following this confirmation, a symmetry analysis was performed to identify any discrepancies between the results and theoretical analysis predictions. The study focused primarily on the high-symmetry path $Z-\Gamma-X$, which spans the valence band maximum fully.

All DFT calculations were carried out using the Quantum ESPRESSO software package. Multiple verification procedures were implemented at various stages of the process to ensure the correctness of the results. After testing alternative software tools, Quantum ESPRESSO was maintained for the post-processing and data analysis steps as it was the only alternative producing physically meaningful results.

The obtained spin textures mostly align with the symmetric expectations. Among the five analyzed paths, only the $Z-\Gamma$ path exhibited complete disagreement with the symmetry analysis. The discrepancy likely originates from the workflow used by Quantum ESPRESSO to generate the system's wavefunctions.

Additionally, a $\vec{k}$-resolved density of states calculation was performed to search for layer localization within the spin-polarized bands. While no layer localization was observed, these results were also used to compute the individual contributions of specific atoms and orbitals within the layers. The resulting atomic contributions were found to be consistent with the constraints imposed by inversion symmetry.

Contents

1 Introduction

Bulk $PdSe_2$ belongs to a family of interesting materials called transition metal dichalcogenides (TMDCs) [1]. These materials possess a wide diversity of unique properties, making them promising candidates within the field of materials science. For instance, they have been utilized in superconductor physics due to their thickness-dependent superconductivity, facilitated by the ease of controlling their thickness via exfoliation [2]. Moreover, these materials have also received attention in optoelectronics, notably as absorbers in solar cells [3]. This can be attributed to TMDC monolayers being highly tunable, enabling better system optimization and the ability to dynamically reconfigure devices.

The search for a hidden persistent spin texture (HPST) in particular is motivated by developments in the field of spintronics. This field aims to utilize the spin of electrons to carry and store information, analogous to the role of electron charge in conventional electronics.
Notable developments in spintronics include spintronic memory devices. Ongoing research suggests these devices could process information faster and have lower energy consumption [4]. This is because spintronic memory devices retain data without the need for continuous power, and spin-orbit effects enable fast, energy-efficient switching of spin currents, giving rise to an energy-efficient configuration. Antiferromagnets have been identified as promising candidates for these applications [5].
Another significant application is the development of nanoscale spintronic oscillators. Spin-based oscillators can be extremely compact, enabling high-density integration in nano devices. This makes them ideal for neuromorphic computing, which aims to mimic the brain's complexity [6]. In addition, they exhibit stable amplitudes due to confinement effects and are highly energy efficient.

The choice of this particular material is noteworthy because it is a layered material that possesses inversion symmetry. Such materials were not considered viable candidates for these effects until about a decade ago, when the concept of hidden effects was popularized. These hidden effects manifest in systems where the global crystal symmetry would seemingly forbid them, yet they exist as they originate from local site symmetry instead. The selection of bulk $PdSe_2$ as a candidate for HPST is motivated by two major factors. First, a recent study by Juan F. Sierra et al. [7] demonstrated that $PdSe_2$ in a graphene heterostructure configuration significantly enhances graphene's spin lifetimes through proximity effects, suggesting the possible existence of an HPST in $PdSe_2$. The effect was found to be highly anisotropic, making it particularly interesting since the spin orientation can be controlled to tune the effect's intensity. Second, the crystal structure of bulk $PdSe_2$ features nonsymmorphic symmetry operations, including a two-fold screw axis rotation that maps the two layers in its unit cell. This operation and its role in generating a hidden spin polarization (HSP) have been discussed in detail by Shan Guan et al. in Ref. [8], indicating $PdSe_2$ could exhibit a similar behavior.

The main objective of this study was to identify and characterize this effect in bulk $PdSe_2$. A specific emphasis was placed on evaluating whether the obtained results agreed with the theoretical constraints imposed on spin expectation values enforced by the crystal's symmetry. The search was performed computationally utilizing first-principles density functional theory (DFT) calculations. Based on these calculations, a spin texture plot was generated to locate the effect. Multiple additional post-processing steps were conducted either as intermediate steps or as complementary results to support the interpretation of the main result. These include a band structure plot, a density of states (DOS) plot, and a momentum-resolved DOS ($\vec{k}$-DOS) calculation. The latter was primarily used to investigate layer localization effects and to resolve individual contributions from specific atoms and orbitals.

2 Theoretical Background

2.1 Density Functional Theory

To search for an HPST in bulk $PdSe_2$, first-principles DFT calculations were used throughout this report. This technique relies on determining an approximation of the solutions to quantum mechanical laws using the electron density of a system as the unknown function, instead of the electron wave function [9].

The foundation of this theory lies in the two Hohenberg-Kohn theorems [10]. The first Hohenberg-Kohn theorem proves that the external potential can be determined solely from the electron density, up to an additive constant. Thereby, the use of electron density as the fundamental variable, as opposed to the wave function, is justified. The second Hohenberg-Kohn theorem states that the electron density that minimizes the total energy of a system corresponds to the ground-state electron density. This means that the ground-state density can be obtained by minimizing the total energy using the variational principle [9].

With this new basis, a solution can be obtained via the Kohn-Sham approach [11]. This involves mapping the many-body interacting system of the material to a Kohn-Sham system, which is a system of non-interacting electrons. The mapping is done under the constraint that the ground-state electron density of the two systems must be the same. As a result, by solving the non-interacting system, the Hamiltonian of the interacting system can be obtained. This Hamiltonian is not exact; aside from the external potential, it includes the kinetic energy of non-interacting electrons and an electron-electron interaction term, which is often approximated. Hence, an additional term called the exchange-correlation functional is added to the Hamiltonian to compensate for this [9]. The exact form of this functional is unknown, representing where the actual approximations begin. A compromise between accuracy and computational cost is made to approximate this functional, depending on the application.

Due to the widespread adoption and well-established reliability of this technique, significant advancements have been made to address increasingly complex scenarios. However, since these are not directly relevant to the material studied in this report, further literature on them can be found in Ref. [9].

2.2 Spin polarization

Spin polarization refers to the phenomenon in which the electron spins preferentially align along a particular direction. Typically, this occurs in ferromagnetic materials, where exchange interactions favor a specific spin orientation [12]. Nevertheless, spin polarization can also occur in nonmagnetic materials via spin-orbit coupling (SOC).

SOC is a relativistic effect that occurs when a moving electron experiences an effective magnetic field due to its motion in the electric field of the nucleus. This causes its spin and orbital degrees of freedom to couple. The resulting interaction influences the electron's energy levels and can induce spin polarization. The role of this effect depends entirely on the system's symmetry. Hence, its types are categorized accordingly.

For materials without inversion symmetry, SOC can induce spin polarization through an effective magnetic field B_{eff} resulting in spin splitting of the electronic bands (Adapted from [13]):

$$B_{eff} = \lambda[\nabla V(\vec{r}) \times \vec{p}] \tag{1}$$

Where $\nabla V(\vec{r})$ is the crystal potential and $\vec{p}$ the momentum.
This splitting occurs when the potential's asymmetry can favor a particular spin orientation. This manifests as two distinct effects depending on the source of the asymmetry: the Dresselhaus (D-1) [14] and Rashba (R-1) [15] effects. For D-1, the asymmetry arises from bulk inversion asymmetry, whereas for R-1 it arises from two-dimensional structural inversion asymmetry.

In centrosymmetric systems with time-reversal symmetry ($\mathcal{T}$), Kramers' theorem [16] guarantees that every eigenstate $|\psi(\vec{k})\rangle$ has a degenerate orthogonal partner due to $\mathcal{T}$ being antiunitary and satisfying $\mathcal{T}^2 = -1$ for spin-$\frac{1}{2}$ particles. Inversion symmetry ($\mathcal{P}$) enforces $E(\vec{k}) = E(-\vec{k})$, ensuring these pairs remain degenerate throughout the entire Brillouin zone. As a result, every band is doubly degenerate at each $\vec{k}$, suppressing the spin splitting caused by SOC. Hence, it was unclear whether spin polarization could even manifest in nonmagnetic inversion-symmetric crystals at all. This was refuted by first-principles calculations in 2014 by Zhang et al. [13], which led to the concept of hidden spin polarization (HSP) through the R-2 and D-2 effects.
The idea is based on the fact that SOC is a relativistic effect, meaning it is rooted in the individual atomic sites in the solid and hence subject to their local point symmetries. Consequently, the total spin polarization of the crystal is just the sum of all atomic site contributions. The key is that the spin polarization due to the hidden D-2 and R-2 effects is spatially localized into different real-space sectors. This means that, for each degenerate band pair, one state in the pair has spin polarization in one real-space sector, while the other state in the pair has the opposite spin polarization but is localized in a different sector.

A spin texture refers to the spatial arrangement and orientation of electron spins within the material's momentum space. In other words, it describes how the spin polarization is spatially distributed in momentum space. Spin textures are categorized in the same way as the spin polarizations mentioned above. Most relevant to this investigation is a particular type of spin texture: persistent spin textures (PSTs). These correspond to spin textures with uniform, momentum-independent spin polarization [17]. Such uniform textures arise due to specific symmetries within the crystal structure. The spin textures investigated in this study should be similar to those generated by hidden Zeeman-type spin polarization (HZSP) [8], given the nature of the materials involved.

2.3 Hidden Zeeman-type spin polarization

HZSP is characterized by a uniform out-of-plane spin configuration within specific crystal planes. In these planes, the degenerate bands exhibit opposite spin orientations perpendicular to the plane, resulting in a net zero spin polarization globally while maintaining local uniform spin polarization within each real-space sector. This sector localization emerges from a nonsymmorphic symmetry that maps these sectors to one another. In the original study by Shan Guan et. al [8], this is enforced by a two-fold screw-axis symmetry along the z-axis:

$$S_{2z} : (x, y, z) \rightarrow (-x, -y, z + \frac{1}{2}) \tag{2}$$

In centrosymmetric materials, it is a combination of this S_{2z} symmetry and inversion symmetry ($\mathcal{P}$) that generates a glide mirror operation giving rise to the PST. For non-centrosymmetric materials, it is a combination of S_{2z} and time reversal symmetry ($\mathcal{T}$) instead. It is the S_{2z} symmetry in particular that protects sector localization, preserving local spin polarization.
The result is this effect's characteristic spin-sectored locking phenomenon, where each band in the degenerate pairs is fixed on the sectors, preventing any spin mixing. The resulting momentum-independent spin polarization consequently exhibits great stability and robustness against external perturbations.
The original study demonstrates this effect through DFT calculations for two material candidates: $WeSe_2$ and $BaBi_4O_7$. Sketches made for WSe_2 to illustrate the HZSP can be found in Figure 1.

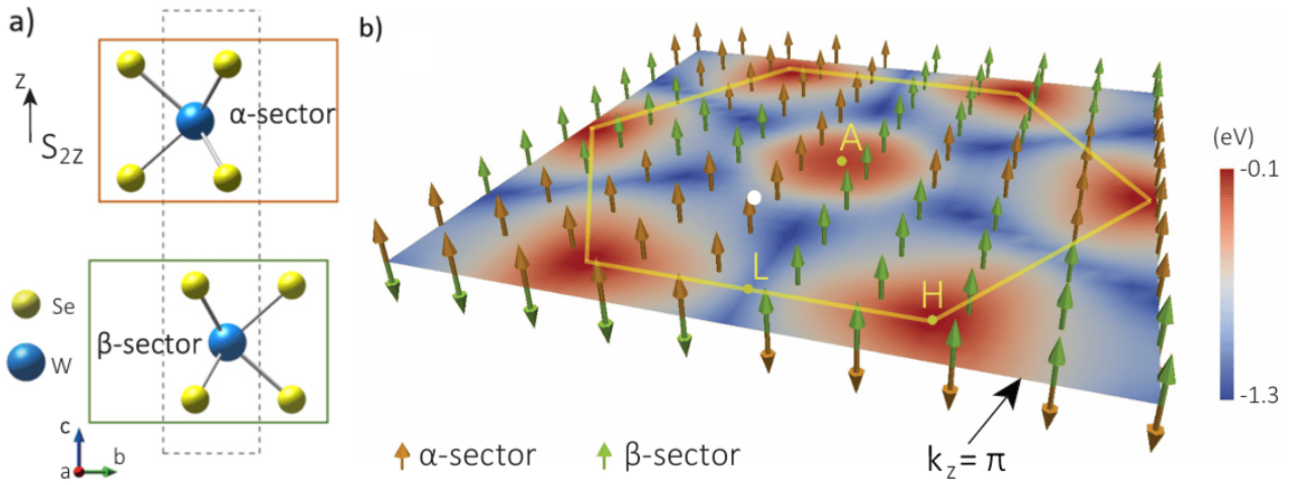

Figure 1: Sketches of the distinct sectors related by S_{2z} symmetry (a) and resulting HZSP (b) of WSe_2. Figures adapted from Ref. [8]

Crucially, the study demonstrates that this effect is solely determined by symmetry, with its location fixed at the Brillouin zone boundary plane. Consequently, materials exhibiting non-symmorphic symmetries that relate two sectors to one another become notable candidates to posses a HPST.

2.4 Symmetry analysis

The regions permitting PSTs within a material can be systematically determined using group theory principles. This approach requires examination of how the symmetry operations at each $\vec{k}$-point constrain the electron spin polarization. As detailed in Ref. [18], this procedure utilizes irreducible representations of type II double magnetic space groups, called grey groups. The analysis is centered around the following formula, which expresses the transformed Pauli matrix components as a linear combination of the original Pauli matrix components:

$$\langle \sigma_\alpha \rangle_{ij} = \langle \psi_i | \, \sigma_\alpha \, | \psi_j \rangle$$

$$\langle \sigma'_\alpha \rangle_{ij} = \sum_{k,k'} D_{ik}(g) D^*_{jk'}(g) \langle \sigma_\alpha \rangle_{kk'} \tag{3}$$

$$\mathrm{D}_{ij}(g) = \langle \psi_i | \, g \, | \psi_j \rangle$$

Here σ_α are the Pauli matrices ($\alpha = x,y,z$), σ'_α are their transformed counterparts and ψ_i are the Bloch states (where $i,j,k,k' = 1,2$ indicating a two-dimensional subspace). $D(g)$ corresponds to the representation of the symmetry group with g being an element of the group.
Solving this equation for all relevant symmetry operations and spin components yields explicit constraints on the allowed Pauli matrix elements. These constraints directly determine the electron spin expectation values [8] (See Equation 4), thereby enabling rigorous prediction of allowed spin polarization directions within the crystal structure.

$$\langle s_\alpha \rangle = \frac{\hbar}{2} \langle \sigma_\alpha \rangle \tag{4}$$

It is essential to note that spin, being a pseudovector, transforms inversely to polar vectors under reflections. This behavior is crucial when analyzing the effect of mirror symmetries on electron spin polarization.

2.5 Material Properties

The material examined in this study is $PdSe_2$, a centrosymmetric layered transition metal dichalcogenide (TMDC). TMDCs are characterized by strong covalent intralayer bonding and weak van der Waals interlayer interactions. TMDCs display remarkable diversity in electronic properties, ranging from semiconducting to metallic, semimetallic, or even superconducting behavior depending on their composition. Furthermore, their properties can be tuned through structural modifications such as varying the layer number or stacking sequence [1]. $PdSe_2$, can exist in both monolayer and bulk forms; however, this study focuses exclusively on the bulk form.

Bulk $PdSe_2$ crystallizes in the Pbca space group (No. 61). This implies $PdSe_2$ has a primitive orthorhombic Bravais lattice and includes non-symmorphic symmetry operations. The unit cell comprises 12 atoms (4 *Pd* and 8 *Se* atoms) arranged in two distinct layers stacked along the crystallographic *c*-axis. Two different views of its structure are presented by Figure 2

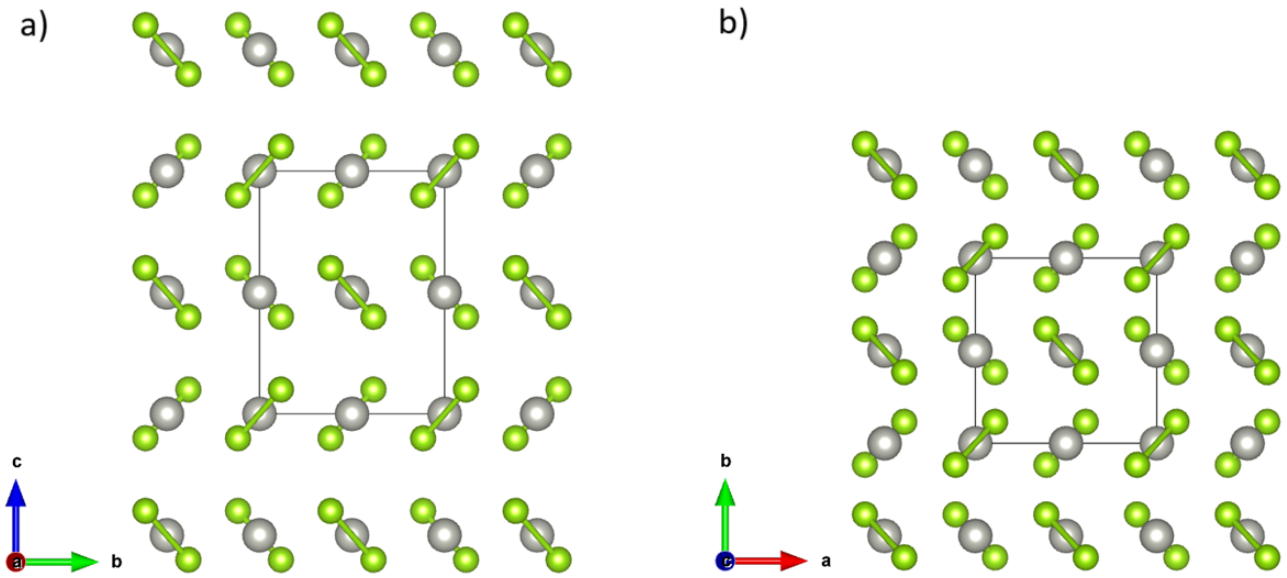

Figure 2: Side view (a) and top view (b) of crystal structure of bulk $PdSe_2$. The solid lines indicate the unit cell.

The complete set of symmetry generators for bulk $PdSe_2$ is provided by Ref. [19]. Notably, it contains inversion symmetry, two-fold screw-axes rotations along all three crystallographic axes, and glide mirrors also along all three axes. The c-axis screw axis rotation (S_2z), maps the two layers in the unit cell to each other, which alludes to similarities with the previously discussed HZSP.

Experimental literature identifies bulk $PdSe_2$ as a non-magnetic semiconductor with an indirect band gap of 0.4eV [20]. First-principles calculations predict it has a positive Seebeck coefficient [**?**], indicating that holes are the dominant charge carriers and that the material exhibits p-type behavior. As a result, the valence band maximum (VBM) is of particular importance and should be closely examined. However, reported DFT calculations by previous studies indicate that the size of the band gap is significantly underestimated in many cases. In some, the material even appears to be a semimetal instead. This is known to occur as a result of the approximations involved in generating the pseudopotentials used for the calculations [21]. Consequently, this discrepancy with the experimental band gap values can be anticipated for this report. Figure 3 illustrates how the band gap is underestimated for two cases.

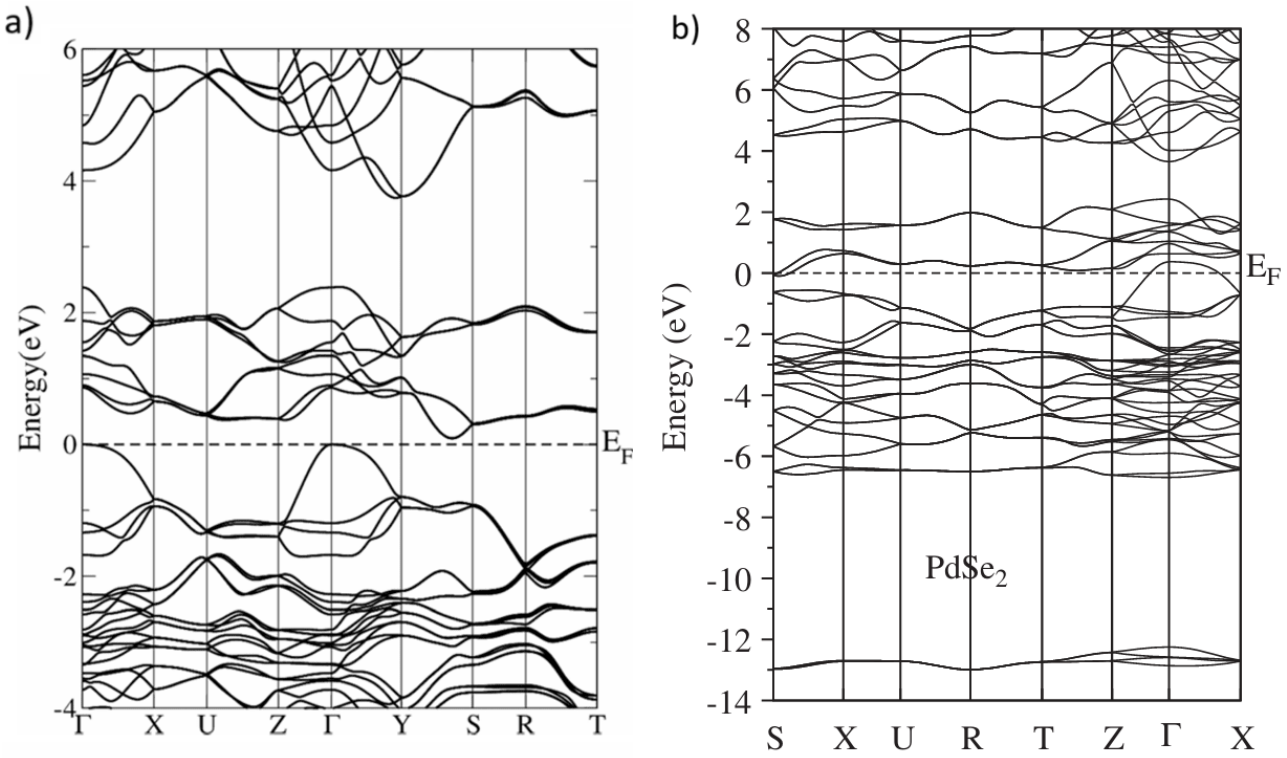

Figure 3: Both figures show the band structure of bulk $PdSe_2$ as determined by literature using DFT calculations. (a) is adapted form [21] and (b) is adapted from [22]

Nevertheless, the search and symmetry analysis of the HPST in this research focused on the valence band maximum (VBM) region, specifically along the high-symmetry $Z-\Gamma-X$ path in the BZ.

3 Methods

3.1 Density Functional Theory Calculations

In this report, the ab initio DFT calculations used to search for the HPST were performed using the Quantum ESPRESSO (QE) [23, 22, 24] software, employing a unified pseudopotential format (UPF). The pseudopotentials (PPs) selected were obtained from the Standard Solid-State Physics (SSSP) collection on the Materials Cloud [25]. Specifically, these were Projector-Augmented Wave (PAW) PPs with an exchange-correlation of the Perdew-Burke-Ernzerhof (PBE) form, found in Pslibrary [26]. The exact names of the selected files are documented in Table 5 in Appendix B.
The wave function cutoff energy (*ecutwfc* parameter) was selected based on convergence tests for the employed pseudopotentials, available on the SSSP collection webpage. All calculations utilized the experimentally determined lattice parameters $a = 5.7457$ Å, $b = 5.8659$ Å and $c = 7.6946$ Å [21].

An initial structural relaxation calculation was performed to determine the ground-state atomic configuration by simultaneously minimizing both the interatomic forces and total energy of the system. This is done by recomputing these values for multiple iterations after shifting the atomic positions slightly until the convergence thresholds are met. The thresholds used for these two parameters were 1×10^{-5} Ry/Bohr and 1×10^{-4} Ry respectively. The starting atomic positions were generated by AFLOW's web entry generator [27]. Given the nature of the calculation, a $8 \times 8 \times 6$ $\vec{k}$-point grid with non-relativistic PPs was used to optimize computational efficiency. The relaxed atomic positions were then used for all remaining calculations.

Subsequently, a Self-Consistent Field (SCF) and a Non-Self-Consistent Field (NSCF) calculation were conducted. The purpose of the SCF calculations was to find the ground-state electronic charge density and total energy of the system by solving the Kohn-Sham equations self-consistently. Then the NSCF calculation could compute the electronic eigenvalues and wavefunctions on a denser $\vec{k}$-point grid without updating the electron density. The sizes of the grids used were $12 \times 12 \times 10$ and $20 \times 20 \times 18$ for each calculation, respectively. Relativistic PPs as well as the *lspinorb* and *noncolin* parameters were employed in both SCF and NSCF calculations to properly account for SOC effects. The NSCF calculation was set to include 252 electronic band states (via the *nbnd* parameter) to ensure sufficient bands were available for the subsequent data analysis.
To ensure the correctness of the calculations, these were repeated to determine the effect of the parameters *nosym*, *noinv*, and *no_t_rev* on the data. This analysis provided valuable insight about whether QE was artificially enforcing degeneracies or incorrectly applying symmetries. This is because, when these parameters are set to true, QE computes everything for each k-point explicitly instead of using symmetries to save computation time.
Additionally, calculations were repeated with a smaller *degauss* parameter to judge its effect on the Fermi level value and the post-processing calculation results. The two values considered were 0.05 and 0.001.

3.2 Post Processing and Data Analysis

For the post-processing calculations, both QE and PAOFLOW [28, 29] were initially considered. The first step was a projection calculation performed using QE, which projects the DFT wavefunctions onto orthogonalized atomic wavefunctions. Band structure and density of states (DOS) plots were computed using QE to confirm that the results of the DFT calculations were accurate when compared

with previously reported DFT calculations. The same test was performed on PAOFLOW to evaluate whether the transformation from plane-wave basis to atomic-orbital basis introduced any issues.

The main calculation evaluated in this study was a band-resolved spin texture calculation conducted along the region of interest $Z-\Gamma-X$. To verify the physical validity of these results, an additional preliminary control calculation was conducted. The chosen path for this calculation was along two points ($P1$ and $P2$) on the $k_z = 0$ plane, intentionally selected to avoid high-symmetry paths. The reduced symmetry along this path simplified the preliminary analysis, which facilitated the verification of the expected symmetry constraints. The positions of $P1$ and $P2$ are shown in Figure 4.

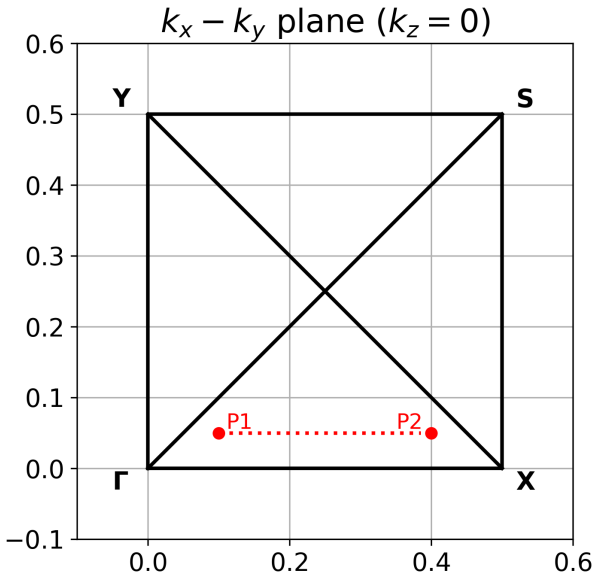

Figure 4: Positions of points $P1$ and $P2$ on the $k_z = 0$ plane

When the correctness of the results was verified using this control test, the main calculation along path $Z-\Gamma-X$ was computed. The calculation was also repeated along a longer path ($S-X-U-R-T-Z-\Gamma-X$) to obtain a broader view of the way QE handled the calculation. The purpose was to have more paths to analyze to support the main results.

A momentum-independent density of states calculation ($\vec{k}$-DOS) was also computed. The results were used to perform a layer projection analysis to investigate whether the degenerate bands at the VBM and those immediately below were localized onto different real-space layers of the crystal. To identify the atomic composition of each layer, the following procedure was used: First, an .xsf file was generated from the SCF input file using XCrySDen [30]. Then, Vesta [31] was used to identify and categorize individual atoms by layer.
The Python script used to analyze this section of the results was adapted from Roy A. [32]. The script was modified to include band-resolved plots among other minor functionalities. The script was very flexible, so numerous other results were also obtained using the $\vec{k}$-DOS data. These included: comparisons of *Pd* contributions against *Se* contributions, orbital-resolved plots, and the determination of individual contributions of all unit cell atoms.

4 Results

4.1 Density Functional Theory Calculations

The relaxed atom positions obtained by the QE relaxation calculation are summarized in Table 1. After confirmation of their validity, these were used for all subsequent calculations.

Table 1: Relaxed atomic positions of the bulk $PdSe_2$ unit cell atoms in crystal (fractional) units, rounded to 3 significant figures.

Atom	x	y	z
Pd	0.000	0.000	0.000
Pd	0.500	0.000	0.500
Pd	0.000	0.500	0.500
Pd	0.500	0.500	0.000
Se	0.108	0.116	0.400
Se	0.392	0.884	0.900
Se	0.892	0.616	0.100
Se	0.608	0.384	0.600
Se	0.892	0.884	0.600
Se	0.608	0.116	0.100
Se	0.108	0.384	0.900
Se	0.392	0.616	0.400

The SCF output file indicated a Fermi energy of 9.5592 eV. The follow-up NSCF calculations output matched this value exactly as expected. Among the numerous tests performed, this result only changed when the *degauss* parameter was lowered from 0.05 to 0.001, yielding a Fermi energy of 9.7969 eV.

4.2 Post-processing Results

The results presented in this subsection correspond exclusively to data generated utilizing QE. That said, most post-processing calculations were also performed with PAOFLOW. All of this data, as well as additional results omitted for conciseness, can be found in Appendix B. In addition, note that most of these results focus particularly on four bands, or at least, some members of this group. These are four key bands along the $Z-\Gamma-X$ path: bands 3 and 4 represent the degenerate pair at the VBM, while bands 1 and 2 constitute the degenerate pair immediately below the VBM.

The post-processing calculations began by verifying the correctness of the DTF calculations. Figure 5 shows the plots obtained for the band structure and DOS calculations used for this purpose.

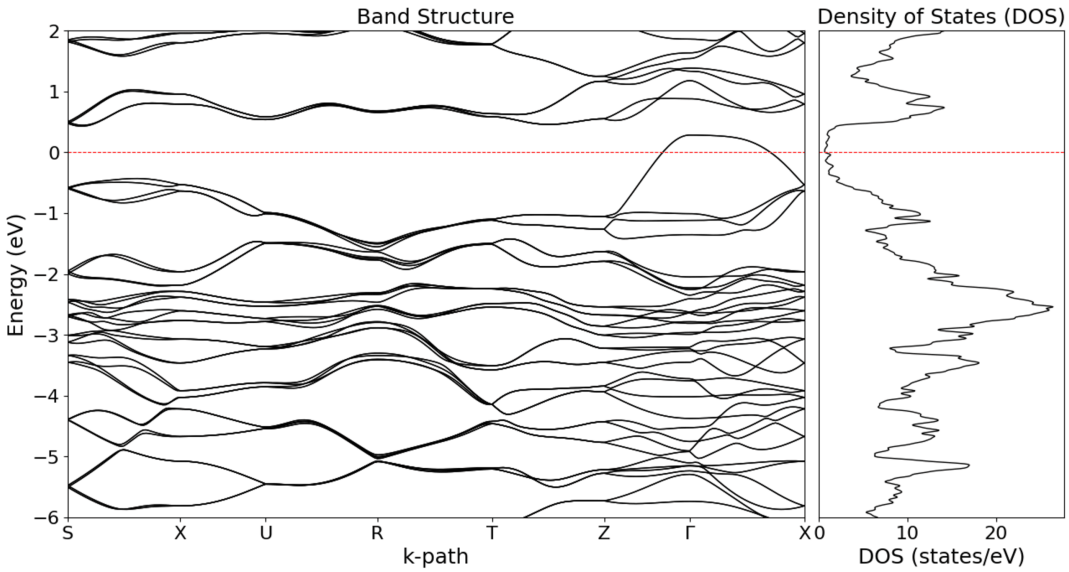

Figure 5: Band Structure along path $S-X-U-R-T-Z-\Gamma-X$ and Density of States (DOS) plot obtained from QE calculations

As mentioned in the methods section, a preliminary symmetry analysis along a path with lower symmetry ($P1-P2$) was made to assess the validity of the spin texture calculations. Figure 6 shows the results obtained for the s_z component along this path. The spin textures for the s_x and s_y components were both negligible.

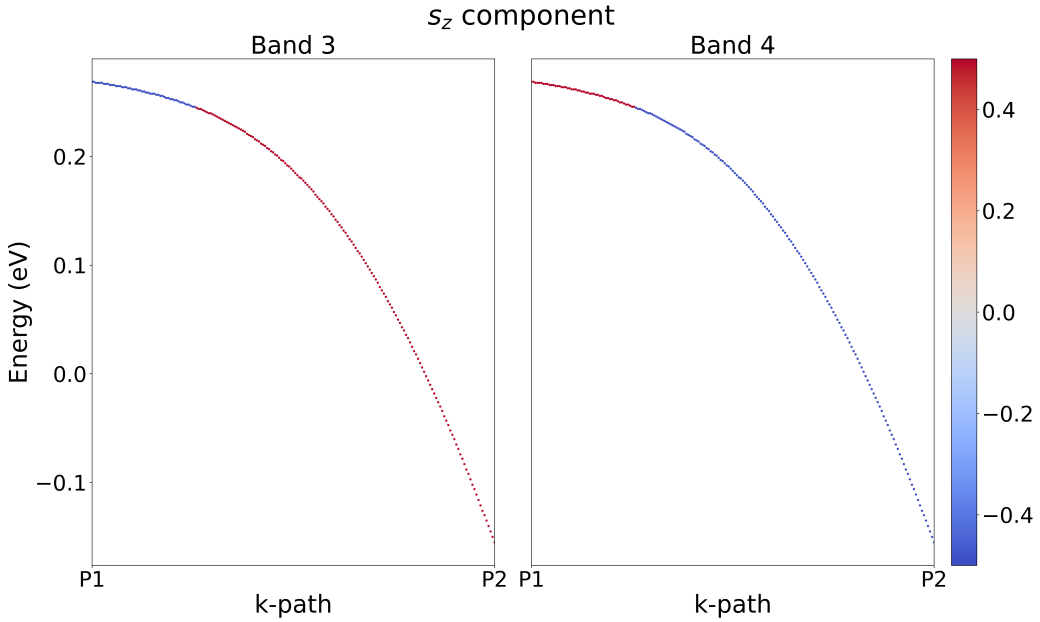

Figure 6: Spin texture for s_z component along $P1-P2$ for bands 3 and 4

The calculation was then computed along the region of interest, path $Z-\Gamma-X$. Figure 7 illustrates the spin textures observed along the s_y component. The spin textures for the s_x and s_z components were negligible despite the appearance of randomly scattered numerical artifacts along the segment $\Gamma-X$.

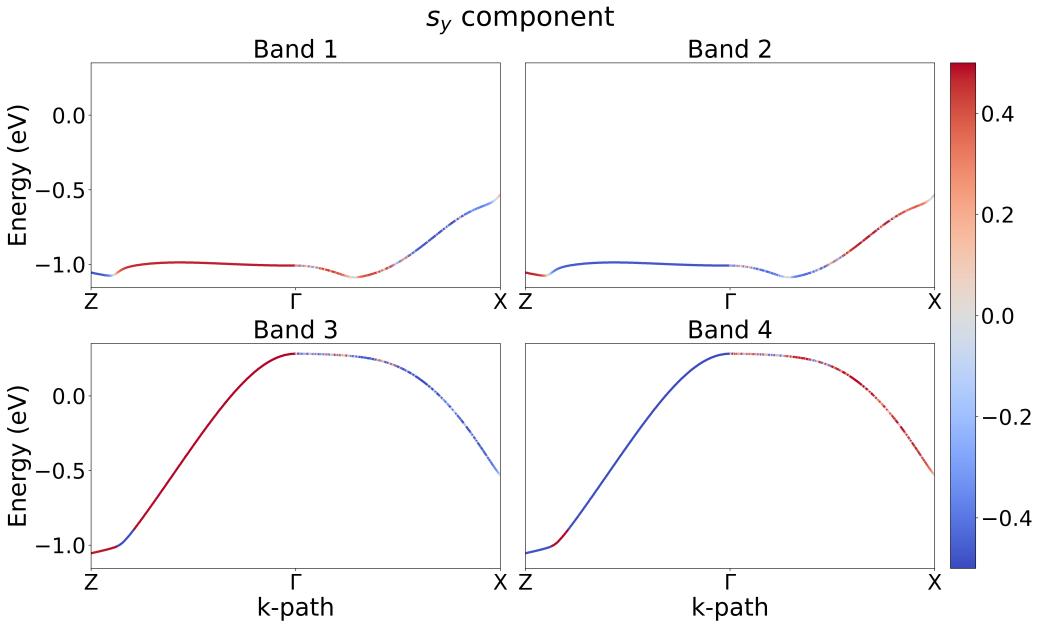

Figure 7: Spin texture for s_y component along $Z-\Gamma-X$ for bands 1-4.

The same procedure was repeated along the longer path $S-X-U-R-T-Z-\Gamma-X$ to obtain a broader collection of the spin textures. These additional paths were considered to complement the results along path $Z-\Gamma-X$. Therefore, the plots obtained are provided in Appendix B for conciseness.

The crystal's structure was analyzed using Vesta to determine the atomic composition of the layers in the unit cell. The atomic composition of the layers is summarized in Table 2. Figure 8 shows the labeled atoms on the unit cell to provide a clearer reference.

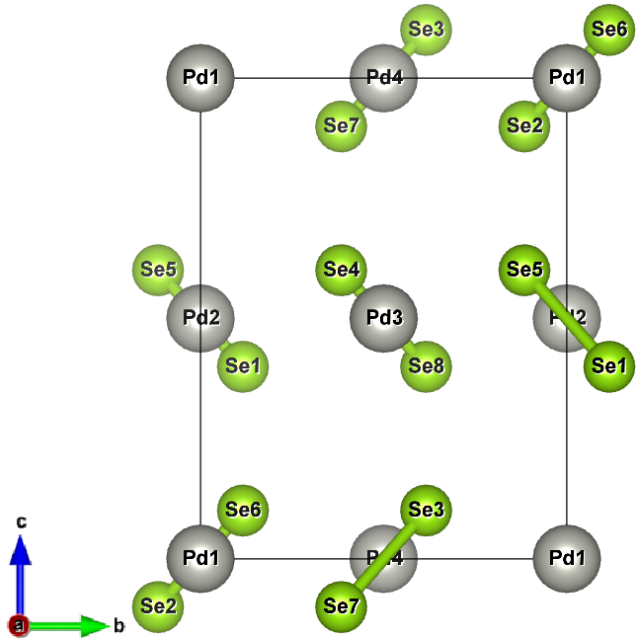

Figure 8: Side view of unit cell of bulk $PdSe_2$ generated using Vesta. The 12 atoms that make up the cell are labeled to illustrate the composition of the two layers.

Table 2: Outlines the atomic composition of the two layers in the unit cell of bulk $PdSe_2$. There are twelve atoms in total, six per layer.

Layer	Atoms
1	Pd1, Pd4, Se2, Se3, Se6, Se7
2	Pd2, Pd3, Se1, Se4, Se5, Se8

Subsequently, the $\vec{k}$-DOS was computed. These results enabled the generation of layer-resolved $\vec{k}$-DOS plots, utilizing the known atomic composition of each layer. No difference was measured between bands forming a degenerate pair for any of the calculations made. For this reason, the figures displaying results for the layer-resolved calculation will show degenerate band pairs being plotted together. For completeness, layer-resolved plots for individual bands are included in Appendix B.

The plots displaying the results observed for the layer-resolved $\vec{k}$-DOS can be found in Figure 9.

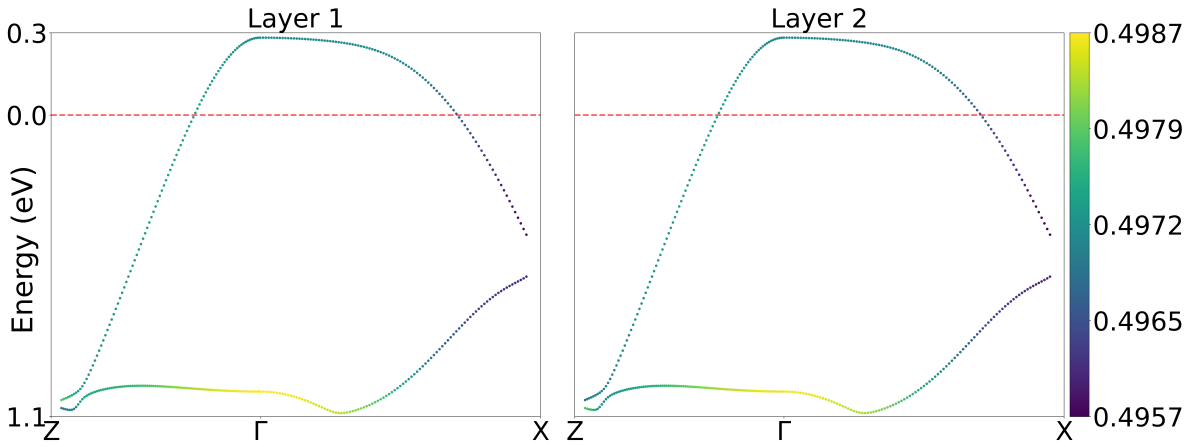

Figure 9: Layer-resolved k-DOS projection plots. For both plots, contributions of bands 1-4 are plotted.

Complementary analyses were performed to characterize individual atomic and orbital contributions. The results revealed distinct band contributions: *Pd* atoms dominated bands 1 and 2, while *Se* atoms primarily contributed to bands 3 and 4, with *Pd* atoms contributing more overall. Orbital decomposition showed nearly exclusive d-orbital character for *Pd* contributions and predominant p-orbital character for *Se* (see Appendix B for supporting figures).

The contributions of all four *Pd* atoms were measured to be identical. On the other hand, for *Se* atoms, there was a small difference between specific *Se* atom pairs within each layer. The pairs with identical contributions were found to be $(Se2, Se6)$ and $(Se3, Se7)$ in layer 1 and $(Se1, Se5)$ and $(Se4, Se8)$ in layer 2. This difference was too small to be conclusively visualized by the subtle color difference in a scatter plot like the ones used above. Nevertheless, this small difference is still consistently reflected by the minimum and maximum DOS contributions per k-point measured for each atom individually. Table 3 displays this information for all *Pd* and *Se* atoms separated by layer.

Table 3: Minimum and maximum $\vec{k}$-DOS contributions for all atoms in the unit cell, separated by layer. The values are highlighted to allow for straightforward recognition of atom group with equivalent contributions.

Atom	Min Weight	Max Weight
Layer 1		
Pd1	0.0881	0.166
Pd4	0.0881	0.166
Se2	0.0134	0.0818
Se3	0.0153	0.0827
Se6	0.0134	0.0817
Se7	0.0153	0.0827
Layer 2		
Pd2	0.0881	0.166
Pd3	0.0881	0.167
Se1	0.0136	0.0820
Se4	0.0118	0.0823
Se5	0.0136	0.0821
Se8	0.0118	0.0823

4.3 Symmetry analysis

This subsection summarizes the constraints obtained for components of the Pauli matrices along all paths considered for the symmetry analyses.

Path $P1-P2$

$$\langle\sigma_x\rangle = \begin{pmatrix} 0 & 0 \\ 0 & 0 \end{pmatrix} \quad \langle\sigma_y\rangle = \begin{pmatrix} 0 & 0 \\ 0 & 0 \end{pmatrix} \quad \langle\sigma_z\rangle = \begin{pmatrix} a & 0 \\ 0 & -a \end{pmatrix} \tag{5}$$

Path $S-X$:

$$\langle\sigma_x\rangle = \begin{pmatrix} a & 0 \\ 0 & -a \end{pmatrix} \quad \langle\sigma_y\rangle = \begin{pmatrix} 0 & 0 \\ 0 & 0 \end{pmatrix} \quad \langle\sigma_z\rangle = \begin{pmatrix} 0 & 0 \\ 0 & 0 \end{pmatrix} \tag{6}$$

Path $R-T$:

$$\langle\sigma_x\rangle = \begin{pmatrix} 0 & 0 \\ 0 & 0 \end{pmatrix} \quad \langle\sigma_y\rangle = \begin{pmatrix} 0 & 0 \\ 0 & 0 \end{pmatrix} \quad \langle\sigma_z\rangle = \begin{pmatrix} 0 & 0 \\ 0 & 0 \end{pmatrix} \tag{7}$$

Path $Z-\Gamma$:

$$\langle\sigma_x\rangle = \begin{pmatrix} a & 0 \\ 0 & -a \end{pmatrix} \quad \langle\sigma_y\rangle = \begin{pmatrix} 0 & 0 \\ 0 & 0 \end{pmatrix} \quad \langle\sigma_z\rangle = \begin{pmatrix} 0 & 0 \\ 0 & 0 \end{pmatrix} \tag{8}$$

Path $\Gamma-X$:

$$\langle\sigma_x\rangle = \begin{pmatrix} 0 & 0 \\ 0 & 0 \end{pmatrix} \quad \langle\sigma_y\rangle = \begin{pmatrix} a & 0 \\ 0 & -a \end{pmatrix} \quad \langle\sigma_z\rangle = \begin{pmatrix} 0 & 0 \\ 0 & 0 \end{pmatrix} \tag{9}$$

5 Discussion

The discussion of the results in this report is divided into two main sections. The first focuses on analyzing the results and reviewing the primary calculations, with emphasis on all intermediate steps performed and the consideration of potential issues within the data. The second section addresses the main question of the report: the existence of HPST in bulk $PdSe_2$. It explores its characteristics and examines the implications of its existence.

5.1 Calculations

Throughout the research process, the results were obtained systematically, verifying their validity before proceeding. This was done through comparison with existing data on bulk $PdSe_2$ when possible. Alternatively, calculations were computed numerous times by experimenting with key parameters. Notably, immediately after the relaxation process, an .xsf file was generated using XCrysden to visualize the obtained relaxed atomic positions. Using VESTA, it was then confirmed that the crystal structure remained unaltered by the systematic atomic position shifts that occur during the relaxation calculation.
Multiple NSCF calculations were repeated by varying the *nbnd* parameter to achieve Fermi energy consistency with SCF results. This procedure prevented potential Fermi level shifts that could arise from including insufficient bands.

Following the DFT calculations, the band structure and DOS plots were used to ascertain the rigor of the DFT results. Cross-validation was performed by comparing the DFT calculation results for bulk $PdSe_2$ with literature data [21, 33]. While the DOS plots showed excellent agreement with published results, the band structure comparison revealed two significant discrepancies. First, the results in Figure 5 show that the band gap is also vastly underestimated for the calculation made in this report. Again, this is a known limitation of the pseudopotentials employed, as discussed in the Theoretical Background section. In addition, minor variations with Ref. [33] appear in band positions near the Fermi level along the $S-X$ path. This is most likely just due to differences in the PPs files used for the calculations.
Moreover, reducing the *degauss* parameter value from 0.05 to 0.001 resulted in a Fermi level shift from 9.559 eV to 9.7969 eV. This is expected as the *degauss* parameter is responsible for setting the smearing width for electronic occupations around the Fermi level. Smearing is a technique used to smooth the convergence of the SCF calculations, as otherwise, convergence can become erratic due to rapidly changing electronic state occupation around the Fermi level. Therefore, larger *degauss* values can cause over-smearing, where too many electrons occupy high-energy states. To maintain the correct total electron count, the Fermi level must be raised to compensate.
None of these systematic discrepancies pose any issues and are not relevant to the rest of the analysis, so they were neglected. Nonetheless, future work could explore alternative functional choices to better reproduce experimental band gaps in bulk $PdSe_2$.

As mentioned in the Methods section, the spin texture calculations were initially assessed using a control calculation and a preliminary symmetry analysis to identify potential issues in the procedure. The control step was implemented after initial concerns emerged regarding recurring band indexing issues in the PAOFLOW results, along with observing significant spin polarization across all spin texture components. The preliminary symmetry analysis was carried out using Equation 3 following the method proposed by Ref. [18], summarized in the theoretical background section.

This specific path ($P1-P2$) was selected for preliminary analysis because it lies along a low-symmetry region, simplifying both computation and interpretation. This approach tested whether the calculation even produces physically meaningful results at all, even in a simple scenario. If discrepancies appeared in this test, their source could be traced more easily compared to more complex configurations. The only relevant symmetries along this path are a non-symmorphic glide mirror operation and a two-fold srew axis operation multiplied by time reversal symmetry. For path $P1-P2$ in particular this are: $\{m_{001}|\frac{1}{2},0,\frac{1}{2}\}$ and $\{2'_{001}|\frac{1}{2},0,\frac{1}{2}\}$. Note that only the rotational part of these operations affects spin, so the translational part is ignored. The irreducible representations (irreps) employed for this analysis were obtained from the Bilbao Crystallographic Server [34]. The results for $P1-P2$ are summarized by Equation 5 (Appendix A shows one example of this type of analysis for reference).

The symmetry analysis confirms that only a non-zero spin texture is allowed for the s_z component. This validation established that solely the QE results exhibited physically meaningful behavior. In contrast, PAOFLOW calculations erroneously produced non-zero spin textures across all components. Notably, there were no apparent band indexing issues in the QE-derived plots obtained along these paths.

The spin texture calculation along the high-symmetry path $Z-\Gamma-X$ does reveal band-indexing artifacts, even in QE-derived plots (See Figure 7). However, instead of emerging in a periodic recurring pattern, these appear to be individual erroneous $\vec{k}$-points randomly scattered along the path. These anomalies have a negligible impact on the overall spin texture analysis due to their sparse distribution. Notably, this only occurs along the $\Gamma-X$ path, and the points become more densely packed close to Γ.

As mentioned in the Methods section, a script created by Roy A. was adapted to analyze and plot the results of the $\vec{k}$-DOS calculation. Before any modifications, the unaltered script was tested to verify its functionality and confirm proper understanding of its workflow. The script was initially designed for plotting orbital-projected band structures of platinum (Pt) from QE calculations. The information about the layers and atoms in bulk $PdSe_2$ was easily implemented, as the script already included a parameter to restrict the plotted states to those corresponding to a specified list of atoms and orbitals. For all plots generated using the $\vec{k}$-DOS results in both QE and PAOFLOW, anomalies were identified at the $\vec{k}$-points at high symmetry points X and Z (start and end of the path). These values were either much larger or smaller than the rest. For instance, for the layer-resolved plots, the average contribution per $\vec{k}$-point was ≈ 0.49 whilst the values at the start and end $\vec{k}$-points were ≈ 0.23 and ≈ 0.77. These anomalies probably occur because four bands converge at these points, implying QE could be mistakenly assigning band contributions in these regions. To prevent this from distorting the plot scales, five $\vec{k}$-points were omitted from both the beginning and end of the path.

5.2 Characterization of the HPST

Figure 7 shows that bulk $PdSe_2$ displays a spin texture along the $Z-\Gamma-X$ path. The s_x and s_z components reveal that the spin texture appears exclusively in the s_y component. Analogous to the symmetry analysis made along the path $P1-P2$, the same procedure was performed for both paths $Z-\Gamma$ and $\Gamma-X$. Table 4 lists the relevant symmetry operations for each path segment, with irreps again obtained from the Bilbao Crystallographic Server.

Table 4: Relevant symmetries along path segments $Z-\Gamma$ and $\Gamma-X$. The full symmetries are listed for completeness, even though only the rotational part is relevant to the analysis.

Path	Relevant symmetries
$Z-\Gamma$	$\{2_{001}\|\frac{1}{2},0,\frac{1}{2}\}$, $\{m_{010}\|0,\frac{1}{2},\frac{1}{2}\}$, $\{m_{100}\|\frac{1}{2},\frac{1}{2},0\}$
	$\{2'_{010}\|0,\frac{1}{2},\frac{1}{2}\}$, $\{2'_{100}\|\frac{1}{2},\frac{1}{2},0\}$, $\{m'_{001}\|\frac{1}{2},0,\frac{1}{2}\}$
$\Gamma-X$	$\{2_{100}\|\frac{1}{2},\frac{1}{2},0\}$, $\{m_{001}\|\frac{1}{2},0,\frac{1}{2}\}$, $\{m_{010}\|0,\frac{1}{2},\frac{1}{2}\}$
	$\{2'_{001}\|\frac{1}{2},0,\frac{1}{2}\}$, $\{2'_{010}\|0,\frac{1}{2},\frac{1}{2}\}$, $\{m'_{100}\|\frac{1}{2},\frac{1}{2},0\}$

The symmetry analysis results for each path segment are summarized by Equation 8 and Equation 9, respectively.
The symmetry analysis for the $\Gamma-X$ path confirms that spin polarization is only permitted along s_y, with degenerate band pairs exhibiting opposite spin polarization. This is in full agreement with the computational spin textures. This result also identifies the randomly scattered erroneous $\vec{k}$-points in the QE-derived plots (Figure 7) as numerical artifacts, since they appear in both s_x and s_z components where symmetry forbids any spin polarization.

In contrast, the $Z-\Gamma$ path analysis indicates spin texture should only appear along s_x, which contradicts the computational results. To identify the nature of this discrepancy, two additional paths were examined ($S-X$ and $R-T$). For path $S-X$, the analysis predicts an s_x-exclusive spin texture, matching the computational results perfectly (See Appendix B). Similarly, no spin texture is allowed at all along the path $R-T$ for any component, in full agreement with the observations.

Overall, out of the six paths chosen, only the results for path $Z-\Gamma$ were contradictory with the symmetry analyses. To examine the source of this issue further, the effect of the *nosym*, *noinv*, and *no_t_rev* parameters was examined for both the SCF and NSCF calculations. The concern was that QE could be assigning symmetries incorrectly, leading to unphysical spin polarizations. The *nosym* parameter prevents QE from using any point-group spatial symmetries during the wavefunction calculations except for time reversal symmetry and magnetic symmetry operations (rotations + time reversal), which are explicitly disabled with *noinv* and *no_t_rev*, respectively. Disabling these symmetries should, in principle, produce identical results, as their primary function is to reduce the number of required $\vec{k}$-points to use explicitly throughout the calculation. To verify this, additional NSCF calculations were performed, systematically testing each parameter's individual effect.
No changes were observed when using either the *noinv* or *no_t_rev* parameters, confirming proper interpretation of both time-reversal symmetry and magnetic symmetry operations. This is supported further by the fact that all bands on the band structure calculations were doubly degenerate everywhere, as expected for a nonmagnetic system with time reversal and inversion symmetry. On the other hand, using *nosym* significantly altered the spin textures computed (See Appendix B). Notably, using this parameter also removed the randomly scattered artifacts along the $\Gamma-X$ path. Despite this, comparisons with the symmetry analysis results show that many of the altered spin textures were completely unphysical. The original results demonstrate significantly better agreement with theoretically allowed spin polarizations. This result implies that QE partially misinterprets spatial point group symmetries, or that disabling these symmetries removes essential physical constraints, generating artificial polarizations. Based on this comprehensive analysis, the original results were preserved, as they most closely align with the allowed spin polarizations predicted.

The root of the issue is likely related to the construction of the degenerate spinor wavefunctions at the NSCF level. Instead of outputting physically meaningful individual spin-polarized eigenstates, QE returns arbitrary linear combinations formed from the states within the degenerate subspace. This choice is not unique, which can lead to the construction of unphysical wavefunction superpositions. In other words, the computed spin expectation values might not correspond to true spin eigenstates, which can lead to unphysical spin textures. Moreover, symmetry has a crucial role in the construction of these superpositions. More symmetries lead to more constraints on the degenerate subspace. This means that when there are fewer constraints, it is easier for QE to produce states closer to representing true physical spin eigenstates. This is observed when comparing the spin textures along the simpler path, $P1-P2$, with the high-symmetry paths. The simpler path only has two relevant symmetries and matches the theoretical expectation flawlessly. The appearance of the numerical artifacts along path $\Gamma - X$ mentioned earlier is probably also closely related to this.

The existence of this issue is understandable, given that the QE software is designed as a general-purpose DFT analysis tool that can be applied flexibly to many types of materials. If this is the case, other software tools that use QE's plane-wave basis projections should also inevitably fail to fully reproduce physical spin texture results. Future research should focus on developing similar software tools specialized for spin-degenerate materials unless this functionality is already implemented elsewhere. This software should explicitly select physically meaningful bases for degenerate wavefunctions rather than relying on arbitrary linear combinations, which are only correct numerically.

Regarding the layer-resolved results, no layer localization is seen, unlike what is suggested by the study of Shan Guan et al. discussed earlier in the theoretical context section [8] (See Figure 9). This was originally surprising given the similarities between bulk $PdSe_2$ and the materials considered in that study. Nonetheless, the results obtained for the individual atom contributions are consistent with the symmetries involved, suggesting the system might behave differently than initially expected.
For instance, by examining the atomic positions of the twelve atoms in the unit cell, it can be seen that *Pd* atoms sit at inversion symmetric sites, meaning their DOS contributions should be equivalent. This is not the case for the *Se* atoms. Instead, *Se* atoms within the layers are related to each other in pairs by inversion symmetry. Consequently, contributions from the *Se* inversion pairs should also be equivalent. The pairs formed this symmetry should be $(Se2, Se6)$ and $(Se3, Se7)$ in layer 1 and $(Se1, Se5)$ and $(Se4, Se8)$ in layer 2. This is precisely what was observed in the $\vec{k}$-DOS results. Given that the difference in contributions is small, the results are presented by recording the minimum and maximum contribution per atom (See Table 3). Despite this, some disagreement arose when the plots for the atomic contributions were closely examined. Small discrepancies were consistently identified near high symmetry points. This heavily suggested the differences were numerical. This was confirmed by computing the individual atomic contribution by maintaining $\vec{k}$-points away from those locations exclusively. The expected results were still reflected by the minimum and maximum contributions for this subset of k-points, confirming the numerical nature of the discrepancy. This discrepancy likely shares the same underlying origin as the unphysical spin polarizations previously discussed.

The next logical step for follow-up studies could be to perform a detailed symmetry analysis following the approach of Shan Guan et al. [8] but for this material instead. The objective would be to evaluate the actual effect of key symmetries, like glide mirrors or $\mathcal{PT}$ symmetry, on the layers and atoms of the material. This analysis would help clarify whether the results obtained by the $\vec{k}$-DOS calculations are truly physical. It would also serve as a rigorous reference to rely on when choosing which atoms to focus on when comparing contributions.

6 Conclusion

In this report, the existence of a hidden persistent spin texture in bulk $PdSe_2$ was verified numerically via DFT calculations. The spin textures obtained were then compared with the result of a symmetry analysis to determine their validity and to identify possible discrepancies.

The framework employed throughout the research process consisted of the following steps. As part of the DFT calculations, relaxation, SCF, and NSCF calculations were performed using QE. For post-processing, PAOFLOW was initially tested but produced unphysical results in preliminary symmetry analysis. Consequently, all post-processing calculations were conducted using QE, including band structure, DOS, spin texture, and $\vec{k}$- DOS computations.
The procedure used to obtain these results followed a highly systematic approach due to the numerous parameters that could potentially introduce errors. Multiple intermediate validation steps were implemented before proceeding to systematically identify discrepancies. These include: verification of the crystal structure following relaxation calculations, repetition of SCF and NSCF calculations varying key parameters, comparison of band structure and DOS plots with existing DFT results for bulk $PdSe_2$, a preliminary symmetry analysis to examine the spin texture over a simple $\vec{k}$-path, and comparative symmetry analyses across multiple high symmetry paths to contrast with results along the primary path. Additional validation was performed for the $\vec{k}$-DOS results, including examination of potential layer localization effects, identification of numerical discrepancies near high-symmetry points, determination of dominant orbital contributions from both *Pd* and *Se* atoms, and comparisons of individual atomic contributions within the crystal layers.

Five distinct symmetry analyses were conducted to validate the spin texture results obtained. Four analyses showed excellent agreement with the results, except for the $Z-\Gamma$ path along the primary path $Z-\Gamma-X$. Specifically, analysis of path $P1-P2$ revealed non-zero spin texture exclusively along the s_z component, while path $S-X$ exhibited spin polarization only along s_x. Path $R-T$ showed a complete absence of spin texture, and path $\Gamma-X$ demonstrated spin polarization exclusively along s_y. The sole discrepancy occurred along path $Z-\Gamma$, where the spin texture was erroneously oriented along s_y rather than the theoretically predicted s_x orientation.
The observed discrepancy likely originates from the wavefunction generation in QE at the NSCF level. QE returns linear combinations of states within the degenerate subspace. The choice for this superposition is not unique, potentially failing to correspond to physically meaningful individual spin-polarized eigenstates. In addition, the results supported the idea that the number of relevant symmetries along the path significantly impacted the manifestation of this issue.

The $\vec{k}$-DOS analysis revealed no evidence of layer localization, in contrast to studies investigating materials with similar conditions. However, detailed examination of atomic contributions within the unit cell demonstrated identical contributions from all *Pd* atoms, while only specific *Se* atom pairs showed equivalent contributions. This observation precisely matches the predicted effects of inversion symmetry on the unit cell: all *Pd* atoms occupy inversion-symmetric sites, whereas *Se* atoms are mapped to partner atoms under this symmetry operation, explaining the observed pairing behavior. A detailed symmetry analysis examining the effects of key symmetry operations on the crystal layers could be used to validate the results and to provide a deeper understanding of what exactly to search for using the $\vec{k}$-DOS results.

Acknowledgments

The author gratefully acknowledges all contributors to this research. Special thanks are extended to Karma for guidance on computational tools and data analysis, to Berkay for theoretical insights and guidance with the symmetry analysis, and to Jagoda for overlooking the project and helping with the discussion of the results.
Gratitude is expressed to the Center for Information Technology at the University of Groningen for technical support and access to the Hábrók high-performance computing cluster. The author also acknowledges the use of Quantum ESPRESSO and PAOFLOW software packages that were essential for the computational work in this study.

Bibliography

[1] R. Lv, J. A. Robinson, R. E. Schaak, D. Sun, Y. Sun, T. E. Mallouk, and M. Terrones, "Transition Metal Dichalcogenides and Beyond: Synthesis, Properties, and Applications of Single- and Few-Layer Nanosheets," *Accounts of Chemical Research*, vol. 48, pp. 56–64, Jan. 2015.

[2] S. Simon, H. Yerzhakov, S. K. P., A. Vakahi, S. Remennik, J. Ruhman, M. Khodas, O. Millo, and H. Steinberg, "The transition-metal-dichalcogenide family as a superconductor tuned by charge density wave strength," *Nature Communications*, vol. 15, p. 10439, Nov. 2024.

[3] B. W. H. Baugher, H. O. H. Churchill, Y. Yang, and P. Jarillo-Herrero, "Optoelectronic devices based on electrically tunable p–n diodes in a monolayer dichalcogenide," *Nature Nanotechnology*, vol. 9, pp. 262–267, Apr. 2014.

[4] J. Puebla, J. Kim, K. Kondou, and Y. Otani, "Spintronic devices for energy-efficient data storage and energy harvesting," *Communications Materials*, vol. 1, p. 24, May 2020.

[5] W. Qi, H. Zhang, L. Chen, A. Du, D. Zheng, Y. Xiao, D. Tian, F. Hu, B. Shen, J. Sun, and W. Zhao, "Antiferromagnetic Spintronics in Magnetic Memory Devices," *IEEE Transactions on Materials for Electron Devices*, vol. 1, pp. 23–35, 2024.

[6] J. Torrejon, M. Riou, F. A. Araujo, S. Tsunegi, G. Khalsa, D. Querlioz, P. Bortolotti, V. Cros, K. Yakushiji, A. Fukushima, H. Kubota, S. Yuasa, M. D. Stiles, and J. Grollier, "Neuromorphic computing with nanoscale spintronic oscillators," *Nature*, vol. 547, pp. 428–431, July 2017.

[7] J. F. Sierra, J. Světlík, W. Savero Torres, L. Camosi, F. Herling, T. Guillet, K. Xu, J. S. Reparaz, V. Marinova, D. Dimitrov, and S. O. Valenzuela, "Room-temperature anisotropic in-plane spin dynamics in graphene induced by PdSe2 proximity," *Nature Materials*, vol. 24, pp. 876–882, June 2025.

[8] S. Guan, J.-W. Luo, S.-S. Li, and A. Zunger, "Hidden Zeeman-type spin polarization in bulk crystals," *Physical Review B*, vol. 107, p. L081201, Feb. 2023.

[9] Nagy, "Density functional. Theory and application to atoms and molecules," *Physics Reports*, vol. 298, pp. 1–79, May 1998.

[10] P. Hohenberg and W. Kohn, "Inhomogeneous electron gas," *Phys. Rev.*, vol. 136, pp. B864–B871, Nov 1964.

[11] W. Kohn and L. J. Sham, "Self-consistent equations including exchange and correlation effects," *Phys. Rev.*, vol. 140, pp. A1133–A1138, Nov 1965.

[12] N. W. Ashcroft and N. D. Mermin, *Solid state physics*. South Melbourne: Brooks/Cole Thomson Learning, repr ed., 2012.

[13] X. Zhang, Q. Liu, J.-W. Luo, A. J. Freeman, and A. Zunger, "Hidden spin polarization in inversion-symmetric bulk crystals," *Nature Physics*, vol. 10, pp. 387–393, May 2014.

[14] G. Dresselhaus, "Spin-Orbit Coupling Effects in Zinc Blende Structures," *Phys. Rev.*, vol. 100, pp. 580–586, 1955.

[15] A. Manchon, H. C. Koo, J. Nitta, S. M. Frolov, and R. A. Duine, "New perspectives for Rashba spin–orbit coupling," *Nature Materials*, vol. 14, pp. 871–882, Sept. 2015.

[16] J. J. Sakurai and J. Napolitano, "Modern quantum mechanics," ch. 4.4, Cambridge: Cambridge University Press, 3rd ed ed., 2021.

[17] L. L. Tao and E. Y. Tsymbal, "Persistent spin texture enforced by symmetry," *Nature Communications*, vol. 9, p. 2763, July 2018.

[18] B. Kilic, S. Alvarruiz, E. Barts, B. van Dijk, P. Barone, and J. Slawinska, "Universal symmetry-protected persistent spin textures in nonmagnetic solids," 2024.

[19] "Bilbao crystallographic server: Table of Space Group Symbols." https://www.cryst.ehu.es/cgi-bin/cryst/programs/nph-getgen, Accessed: 2025-06-14.

[20] J. Wilson and A. Yoffe, "The transition metal dichalcogenides discussion and interpretation of the observed optical, electrical and structural properties," *Advances in Physics*, vol. 18, pp. 193–335, May 1969.

[21] C. Soulard, X. Rocquefelte, P.-E. Petit, M. Evain, S. Jobic, J.-P. Itié, P. Munsch, H.-J. Koo, and M.-H. Whangbo, "Experimental and theoretical investigation on the relative stability of the pds2- and pyrite-type structures of pdse2," *Inorganic Chemistry*, vol. 43, no. 6, pp. 1943–1949, 2004. PMID: 15018514.

[22] P. Giannozzi, S. Baroni, N. Bonini, M. Calandra, *et al.*, "Quantum espresso: a modular and open-source software project for quantum simulations of materials," *Journal of Physics: Condensed Matter*, vol. 21, no. 39, p. 395502 (19pp), 2009.

[23] P. Giannozzi, O. Andreussi, T. Brumme, O. Bunau, *et al.*, "Advanced capabilities for materials modelling with quantum espresso," *Journal of Physics: Condensed Matter*, vol. 29, no. 46, p. 465901, 2017.

[24] P. Giannozzi, O. Baseggio, P. Bonfà, D. Brunato, *et al.*, "Quantum espresso toward the exascale," *The Journal of Chemical Physics*, vol. 152, no. 15, p. 154105, 2020.

[25] G. Prandini, A. Marrazzo, I. E. Castelli, N. Mounet, and N. Marzari, "Precision and efficiency in solid-state pseudopotential calculations," *npj Computational Materials*, vol. 4, no. 1, p. 72, 2018. http://materialscloud.org/sssp.

[26] Q. E. Team, "Pslibrary: The quantum espresso pseudopotential library," 2019. Accessed: 2025-04-26.

[27] "AFLOW materials Page, PdSe2 (icsd 170327)." https://aflowlib.duke.edu, Accessed: 2025-04-26.

[28] F. T. Cerasoli, A. R. Supka, A. Jayaraj, M. Costa, I. Siloi, J. Sławińska, S. Curtarolo, M. Fornari, D. Ceresoli, and M. Buongiorno Nardelli, "Advanced modeling of materials with PAOFLOW 2.0: New features and software design," *Computational Materials Science*, vol. 200, p. 110828, Dec. 2021.

[29] M. Buongiorno Nardelli, F. T. Cerasoli, M. Costa, S. Curtarolo, R. De Gennaro, M. Fornari, L. Liyanage, A. R. Supka, and H. Wang, "PAOFLOW: A utility to construct and operate on ab initio Hamiltonians from the projections of electronic wavefunctions on atomic orbital bases, including characterization of topological materials," *Computational Materials Science*, vol. 143, pp. 462–472, Feb. 2018.

[30] A. Kokalj, "Xcrysden—a new program for displaying crystalline structures and electron densities," *Journal of Molecular Graphics and Modelling*, vol. 17, no. 3-4, pp. 176–179, 1999.

[31] K. Momma and F. Izumi, "Vesta 3 for three-dimensional visualization of crystal, volumetric and morphology data," *Journal of Applied Crystallography*, vol. 44, no. 6, pp. 1272–1276, 2011.

[32] A. Roy, "Projected bands in quantum espresso: Spin-orbit coupling for pt." `https://github.com/AdityaRoy-1996/Projected-Bands-in-Quantum-Espresso/tree/main/Spin_Orbit/Pt`, 2024. Accessed: 2025-05-27.

[33] A. Hamidani, B. Bennecer, and K. Zanat, "Structural and electronic properties of the pseudo-binary compounds PdX2 (X=P, S and Se)," *Journal of Physics and Chemistry of Solids*, vol. 71, pp. 42–46, Jan. 2010.

[34] L. Elcoro, B. J. Wieder, Z. Song, Y. Xu, B. Bradlyn, and B. A. Bernevig, "COREPRESENTATIONS: Irreducible co-representations of magnetic double space groups." Bilbao Crystallographic Server, 2020. Accessed: 2025-06-18.

Appendices

A Calculations

Equation 10 presents a representative case of the symmetry analysis performed in this study. Specifically, the example illustrates the constraints obtained for the diagonal elements of the Pauli matrices arising from the glide mirror operation $\{m_{001}|\frac{1}{2},0,\frac{1}{2}\}$ along the path $\Gamma - X$.

$$
\begin{gathered}
m_{001} : (\sigma_x, \sigma_y, \sigma_z) \rightarrow (-\sigma_x, -\sigma_y, \sigma_z) \\
D(m_{001}) = \begin{pmatrix} 0 & e^{i\pi(-1+2u)/2} \\ e^{i\pi(-1+2u)/2} & 0 \end{pmatrix} \\
\langle \sigma'_\alpha \rangle_{11} = \sum_{k,k'} D_{1k}(m_{001}) D^*_{1k'}(m_{001}) \langle \sigma_\alpha \rangle_{kk'} = D_{12}(m_{001}) D^*_{12}(m_{001}) \langle \sigma_\alpha \rangle_{22} \\
\langle \sigma'_\alpha \rangle_{11} = \langle \sigma_\alpha \rangle_{22} \\
\text{Therefore: } \langle \sigma_x \rangle_{11} = -\langle \sigma_x \rangle_{22},\ \langle \sigma_y \rangle_{11} = -\langle \sigma_y \rangle_{22},\ \langle \sigma_z \rangle_{11} = \langle \sigma_z \rangle_{22}
\end{gathered}
\tag{10}
$$

B Raw Data

Table 5 contains the exact PP file names used throughout this study.

Table 5: Explicit pseudopotential files used for all calculations presented by this report

Pseudopotential Filenames
Pd.pbe-n-kjpaw_psl.1.0.0.UPF
Pd.rel-pbe-n-kjpaw_psl.1.0.0.UPF
Se.pbe-dn-kjpaw_psl.1.0.0.UPF
Se.rel-pbe-dn-kjpaw_psl.1.0.0.UPF

A link to a folder containing all additional results obtained from both QE and PAOFLOW:
PdSe2 Raw Data